

# Interaction of dual sweeping impinging jets at different Reynolds numbers

Xin Wen, Ziyang Li, Wenwu Zhou, and Yingzheng Liu

Citation: *Physics of Fluids* **30**, 105105 (2018); doi: 10.1063/1.5054161

View online: <https://doi.org/10.1063/1.5054161>

View Table of Contents: <http://aip.scitation.org/toc/phf/30/10>

Published by the *American Institute of Physics*

---

---

**PHYSICS TODAY**

WHITEPAPERS

## ADVANCED LIGHT CURE ADHESIVES

Take a closer look at what these environmentally friendly adhesive systems can do

READ NOW

PRESENTED BY  
**MASTERBOND**  
ADHESIVES | SEALANTS | COATINGS

# Interaction of dual sweeping impinging jets at different Reynolds numbers

Xin Wen,<sup>1,2</sup> Ziyang Li,<sup>1,2</sup> Wenwu Zhou,<sup>1,2</sup> and Yingzheng Liu<sup>1,2,a)</sup>

<sup>1</sup>Key Lab of Education Ministry for Power Machinery and Engineering School of Mechanical Engineering, Shanghai Jiao Tong University, 800 Dongchuan Road, Shanghai 200240, China

<sup>2</sup>Gas Turbine Research Institute, Shanghai Jiao Tong University, 800 Dongchuan Road, Shanghai 200240, China

(Received 30 August 2018; accepted 5 October 2018; published online 24 October 2018)

Dual sweeping impinging jets emerging from a synchronized pair of fluidic oscillators were experimentally measured using time-resolved particle image velocimetry in a water tank. Interestingly, distinct behaviors of the dual jets were observed at three different Reynolds numbers. At the lowest Reynolds number  $Re = 1.8 \times 10^3$ , the dual jets can be generally treated as two isolated jets with a good in-phase sweeping motion and a relatively stable jet velocity. One pair of wall vortices develops and interacts in a trade-off manner in the middle region between the two jets. In the time-averaged flow fields close to the wall, each jet generates one major peak value of streamwise velocity and one pair of peak values (positive and negative) of transverse velocity laterally along the wall. The turbulence fluctuations in both directions also have peak values laterally. In the transverse direction, the velocity also has high turbulence fluctuations in the middle region between the two jets caused by the wall vortices. At the highest Reynolds number  $Re = 9.2 \times 10^3$ , the dual jets experience significantly distorted oscillation patterns and strong variations in their jet velocity during one actuation cycle. The dynamic behavior, the induced wall vortices, and the resulting time-averaged impingement of the dual jets are, in essence, very similar to the sweeping jet that would be produced from a single, but bigger, oscillator. At the intermediate Reynolds number  $Re = 5.5 \times 10^3$ , the performance of the dual sweeping jets is at the transition stage. *Published by AIP Publishing.* <https://doi.org/10.1063/1.5054161>

## I. INTRODUCTION

As one of the most efficient methods of enhancing heat transfer along solid walls, impinging jets have widespread applications in gas turbines, chip cooling, and metallurgy. Multiple jets are usually applied, with the aim of yielding a broad impact region and a uniform distribution of heat transfer along the wall (Geers *et al.*, 2005 and Wen *et al.*, 2017). However, straight impinging jets are characterized by a substantial elevation of heat transfer in the impingement spot but rapid attenuation of the heat transfer being away. In a configuration with multiple jets, neighboring jets often collide in the space between them, hindering local heat transfer. A novel fluidic actuator generating a strongly periodic sweeping jet would thus be a very favorable mechanism to broaden the wall coverage of the jet (Agricola *et al.*, 2017 and Park *et al.*, 2018), while multiple sweeping jets with phase synchronization have great potential to bring flow phase-resolved on into the convective heat transfer due to the in-phase oscillation. As a first attempt at creating phase-synchronized dual sweeping impinging jets, flow dynamics and the resulting spatial distribution of the impingement along a flat wall are the focus of the current study.

The flow dynamics and superimposed vortical structures of single straight impinging jets have been the focus of a great deal of research (Fairweather and Hargrave, 2002; Vejrazka *et al.*, 2005; Geers *et al.*, 2005; Hadžiabdić and Hanjalić, 2008; New and Long, 2015; and Chatterjee and Fabris, 2017).

These studies have already established a common perception of a simple round jet impinging steadily upon a flat wall perpendicularly. As shown in Fig. 1, this implies that the flow field can be divided into three distinct regions: the free-jet, a stagnation region, and the wall-jet region (Guo *et al.*, 2017 and Yadav and Agrawal, 2018). Terzis (2016) correlated the flow dynamics and enhanced heat transfer by using both particle image velocimetry (PIV) and thermochromic liquid crystals (TLCs) to measure the flow field and local heat transfer rate, respectively. He found a close correlation between the streamwise velocity component and the primary peak values of heat transfer in the stagnation region. In the wall-jet region, he observed that wall vortices were responsible for the appearance of the secondary peak value of the heat transfer rate, as a result of enhanced turbulence fluctuations. Hubble *et al.* (2013) also revealed that downwash and upwash flows induced at different branches of the wall vortices can enhance and hinder the heat transfer, respectively.

The flow fields induced by multiple impinging jets are further complicated by interactions between them. Multiple jets are usually used with the aim of yielding a more uniform distribution of the heat transfer along the wall. However, the interaction between neighboring jets can bring new elements of non-uniformity. As shown in Fig. 1, a secondary stagnation region with an upwash flow may appear in the space between the jets, hindering the impingement effect (Can 2003; Hewakandamby, 2009; and Chander and Ray 2007). For this reason, unsteady jets with optimized phase differences are introduced, including pulsed jets (Hewakandamby, 2009 and Farahani *et al.*, 2016) and synthetic jets (Greco *et al.*, 2016;

<sup>a)</sup>Author to whom correspondence should be addressed: yzliu@sjtu.edu.cn

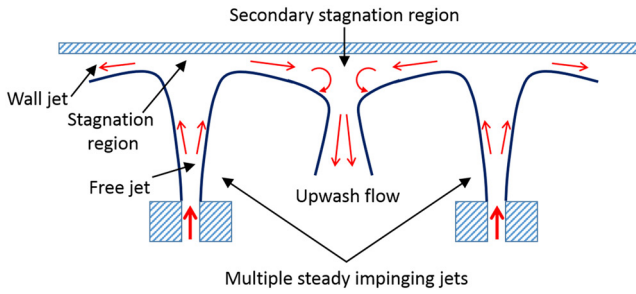


FIG. 1. Schematic diagram of multiple jet impingement.

Feng *et al.*, 2011; Feng and Wang, 2014; Xu *et al.*, 2013; and 2017), which can provide enhanced and more homogeneous heat transfer. However, the actuators rely on either mechanical or piezoelectrical moving parts to produce unsteady jets, which in return have limitations in actuating frequency, operational life span, and applications in high-Reynolds-number conditions.

Recently, sweeping jets issued from a fluidic oscillator have shown increasing potential in applications of impingement (Camci and Herr, 2002; Tesaf, 2009; Lundgreen *et al.*, 2017; Agricola *et al.*, 2017; and Park *et al.*, 2018). Unlike other unsteady jet actuators, the fluidic oscillator requires no moving parts and relies only on internal flow dynamics to produce a transverse sweeping jet. Inside the oscillator, the main jet is attracted to one sidewall due to the Coanda effect; opening a feedback channel on the wall will direct parts of the jet flow back to the inlet, causing the jet to flip to the other side (Bobusch *et al.*, 2013; Ostermann *et al.*, 2015; and Wen and Liu, 2018). A number of studies have also been conducted recently to explore the external flow characteristics of the sweeping jets. From the perspective of impingement application, oscillation patterns, including the jet sweeping motion and jet velocity, are particularly interesting as these are directly related to the impingement effect along the wall. Koklu (2016) found that an extended jet exit can significantly increase the jet maximum spreading angle of its sweeping motion, due to the Coanda effect between the jet and the exit wall. Using air under room temperature, Woszidlo *et al.* (2015) showed that a larger maximum spreading angle can yield an uneven time-averaged spatial distribution of jet momentum. Previous time-resolved PIV (TR-PIV) measurements in a water tank revealed that the jet maximum spreading angle can also increase with increasing Reynolds number ranging between  $Re = 2 \times 10^3$  and  $12 \times 10^3$  (Wen *et al.*, 2018 and Wen and Liu, 2018). With a larger maximum spreading angle, the jet velocity is obviously higher on the lateral outer sides than around the centerline of the actuator. This further leads to non-uniform impingement on a flat wall which is  $8D_h$  from the jet exit, where  $D_h$  is the hydrodynamic diameter of the jet exit. In addition, similar to a steady impinging jet, sweeping jets can also induce lateral wall vortices, causing notable turbulence fluctuations. The ability of sweeping impinging jets to enhance heat transfer due to their distinct flow dynamics has also been proved. By experimental comparison using hot air, Tesaf (2009) observed a substantial enhancement in heat transfer induced by sweeping jets compared with steady jets, with an increase of up to 200%. This superior capability of sweeping jets was also confirmed

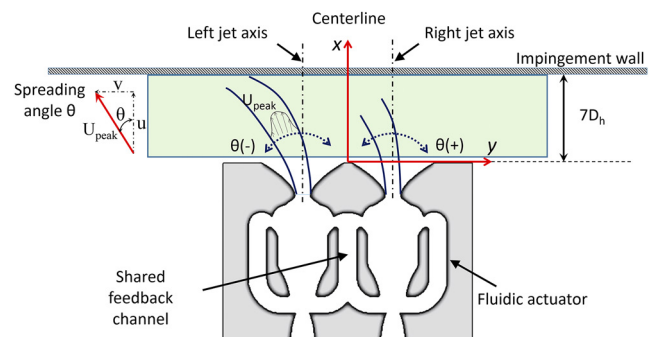
by a more recent study by Park *et al.* (2018) using hot air within a range of  $3.6 \times 10^3 < Re < 15.3 \times 10^3$ . In an air thermal chamber, Agricola *et al.* (2017) found that sweeping jets can also provide a more uniform impingement than a circular steady jet. To the best of the authors' knowledge, most previous efforts have been concentrated on a single sweeping jet. No attempt has been made to explore detailed interactions between multiple sweeping jets in the impingement process.

In the current study, dual sweeping impinging jets emerging from a synchronized pair of fluidic oscillators were applied in jet impingement upon a flat wall. By taking advantage of the Coanda effect, this design can yield a jet maximum spreading angle of up to  $90^\circ$ . The wall was then fixed at  $7D_h$  from the jet exits to allow for sufficient jet coverage, where  $D_h$  is 3 mm. This distance also falls in the most effective range for jet impingement, i.e., within  $10D_h$  (Tesaf, 2015). TR-PIV measurements were made in a water tank using distilled water under room temperature ( $24^\circ\text{C}$ ) and pressure to examine the interactions between the dual sweeping impinging jets under different Reynolds numbers. Three Reynolds numbers were selected for detailed examination, i.e., at  $Re = 1.8 \times 10^3$ ,  $5.5 \times 10^3$ , and  $9.2 \times 10^3$ , based on  $D_h$  and the exit velocities ( $U_{SJ} = 0.6, 1.9, \text{ and } 3.1 \text{ m/s}$ , respectively). Oscillation patterns, interactions of the wall vortices, and time-averaged impingement performance along the wall were then examined in detail and compared.

## II. EXPERIMENTAL APPROACHES

### A. Optimized design of fluidic oscillator pair

Due to the nature of self-induced oscillation, multiple sweeping jets without synchronization can lead to destructive collision between jets along an impingement wall when these are out of phase. Recently, Tomac and Gregory (2017) proposed a new design of a fluidic oscillator pair. By sharing inner feedback channels, the oscillator pair was demonstrated to produce dual sweeping jets with an in-phase motion, as shown in Fig. 2. Although very interesting, their design was limited by the jet maximum spreading angle, which was restricted to below  $40^\circ$ . As the transverse distance between the side-by-side oscillators was fixed, the dual sweeping jets had to travel a long

FIG. 2. Schematic diagram of the dual sweeping impinging jets. The green-filled, blue-outlined region indicates the field of view, which spans  $y = \pm 16D_h$  and  $x = 0.7D_h \sim 7D_h$ .

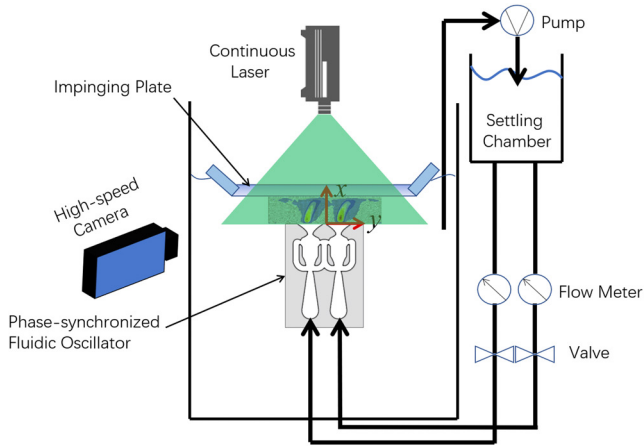


FIG. 3. Sketch of experimental setup (not to scale).

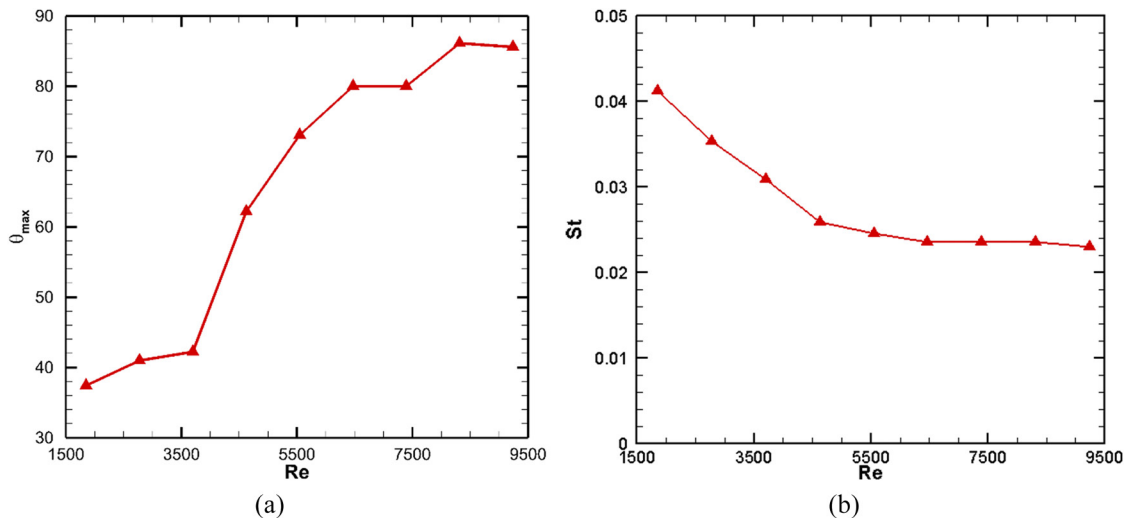
distance from the exits in the streamwise direction before covering the middle region between them. This requires that the impingement wall is far away from the jet exits, which is far beyond the most suitable range for jet impingement, which should be within  $10D_h$  (Tesař, 2015). In the current study, to expand the maximum spreading angle, the exits of the actuators were specially designed to have a curved shape and were extended in length as much as possible within the geometrical limitations, as shown in Fig. 2. With this new design, both jets have a maximum spreading angle of up to  $90^\circ$ . As such, by placing a wall  $7D_h$  from the exits, the jets can well cover the middle region. The optimized fluidic actuator pair was then placed inside the water tank used in the authors' previous studies (Wen *et al.*, 2018 and Wen and Liu, 2018). Then, by controlling the jet flow rate, a total of nine Reynolds numbers ranging from  $1.8 \times 10^3$  to  $9.2 \times 10^3$  were obtained.

As shown in Fig. 2, the coordinate system is set along the exit surface. The origin point is at the center between the two exits. The  $x$  axis is pointing in the streamwise direction, with the  $y$  axis in the transverse, i.e., sweeping, direction. The centerline of each actuator is at  $y = \pm 4.7D_h$ . As shown in Fig. 2, the spreading angle  $\theta$  was obtained from the  $u$  (in the

streamwise direction,  $x$ ) and  $v$  (in the transverse direction,  $y$ ) components of the peak velocity magnitude in the jet column in the near-exit region (Wen and Liu, 2018). It has a negative peak value when the jet is most deflected to the left side, and a positive peak value to the right.

## B. TR-PIV measurement

For the TR-PIV measurement, glass beads with a density of  $\rho \approx 1050 \text{ kg/m}^3$  and a diameter of  $d \approx 20 \mu\text{m}$  were seeded throughout the water tank as tracer particles. Before PIV measurement, the air bubbles in the jet pipes were carefully removed. As shown in Fig. 3, a 5-W continuous-wave laser with a wavelength of 532 nm (MGL-N-532a-5w, CNI) was used to generate a laser sheet of about 1 mm thickness by passing through integrated optics. The laser was fired from the top to bottom and lit the area of interest by passing through a transparent impingement wall with a thickness of 3 mm and made by plexiglass. A high-speed camera (dimax HS4, pco.) was applied to capture images in the area of interest, which spanned  $y = \pm 16D_h$  and  $x = 0.7D_h \sim 7D_h$  as shown in Fig. 2. With a total of  $952 \times 190$  effective pixels in the present measurement, a resolution of about 0.1 mm/pixel was yielded. Note that the region very close to the jet exit wall was excluded due to the limitation of PIV measurements (for example, the laser reflection). The instantaneous maximum velocity within the measurement area was about 3.5 m/s. Due to distinct jet frequencies at different Reynolds numbers, the sampling rate of the camera and measurement duration were also dynamically adjusted to resolve at least 1/100th of the sweeping frequency and cover 50 sweeping cycles, respectively. To obtain a vector map from the particle images, a PIV software package, Micro-Vec (PIVtec, China), was employed; a multigrid cross-correlation technique (Raffel *et al.*, 2013), in combination with subpixel recognition by Gaussian fitting (Yasuhiko *et al.*, 2000), was used. A final interrogation window of  $16 \times 16$  pixels and 50% overlap gave rise to spatial resolution 0.7 mm of the vectors. The uncertainty in the velocity was estimated as approximately 2%, based on the size of the interrogation window, sampling rate, and particle density

FIG. 4. Overall performance of the single jet plotted against the Reynolds number: (a) maximum spreading angle  $\theta_{max}$  and (b) Strouhal number  $St$ .

(Wen *et al.*, 2015). Details of the experiment can be found in the authors' previous study (Wen *et al.*, 2018).

### C. Phase averaging and time frame

To obtain phase-resolved oscillation patterns and interaction details between the jets, the corresponding phase

indicators were obtained with the help of time-resolved instantaneous flow fields. Two specific locations in the flow fields were selected to extract velocity differences. A numerical low-pass filter and a cross-correlation algorithm were then applied to the time-dependent velocity difference to obtain phase indicators. In the phase-averaged process, the whole

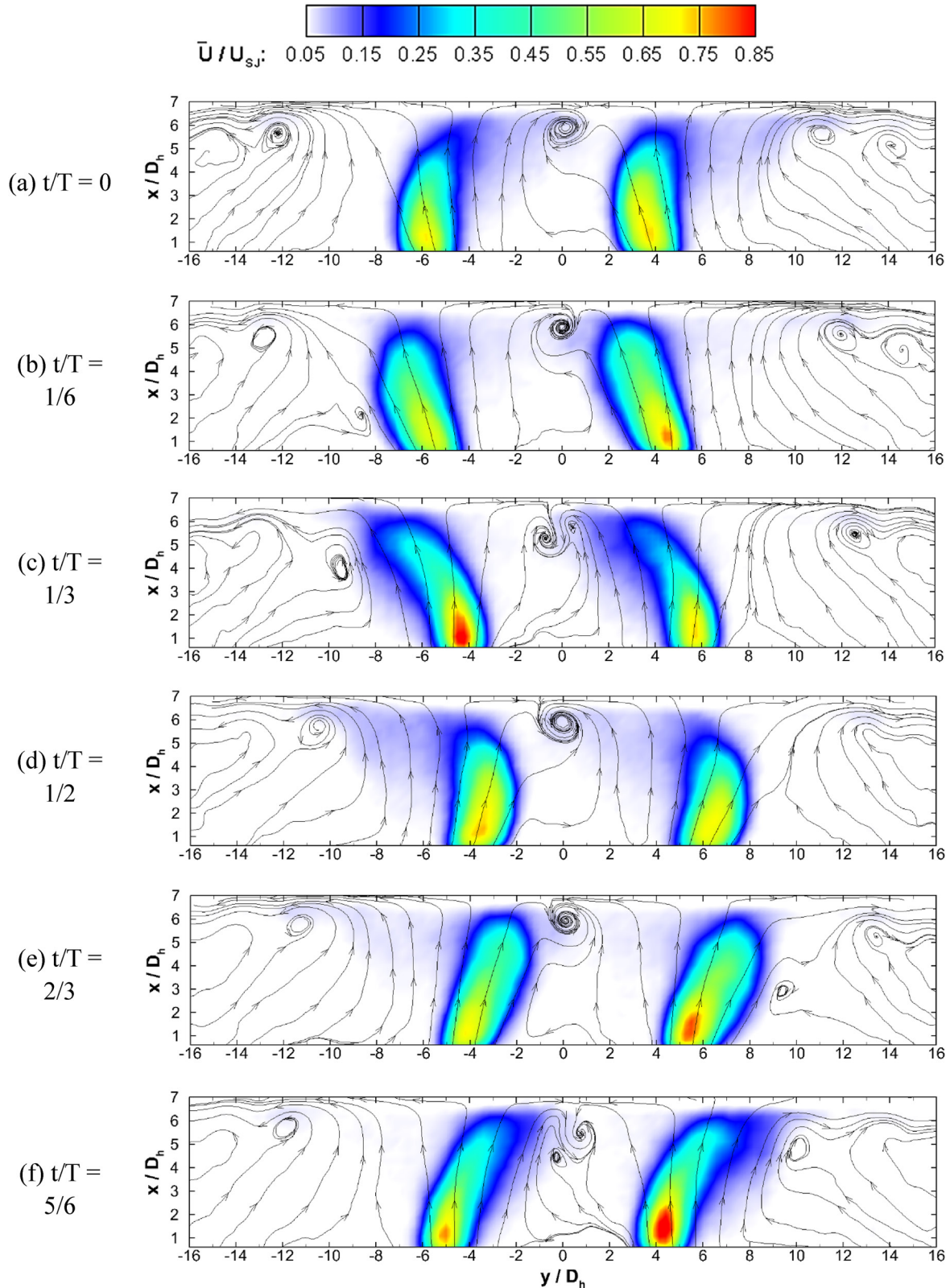


FIG. 5. Sweeping motions of the dual jets shown by contours of phase-averaged velocity magnitude with streamlines at  $Re = 1.8 \times 10^3$ .

cycle of the dual sweeping jet system was divided into 120 phases. This resulted in at least 500 instantaneous flow fields within an interval of  $3^\circ$ . Details of this phase-averaging method can be found in previous studies (Ostermann *et al.*, 2015; Wen *et al.*, 2018; and Wen and Liu, 2018). The establishment of the time frame requires special attention due to the jet's possible distorted sweeping motions. After careful consideration, the oscillation of the dual-jet system was set to begin when the right jet reached its most leftward position in the middle region between the two jets.

### III. RESULTS AND DISCUSSION

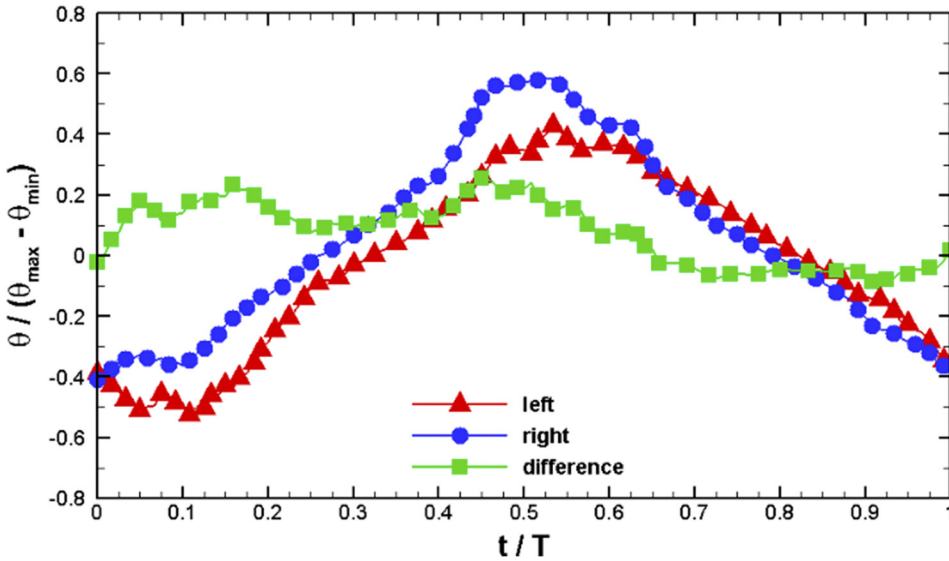
#### A. Overall performance of single jet

Dual jets were first isolated from each other to examine the dependencies of the jet maximum spreading angle  $\theta_{max}$  and frequency  $f$  on the Reynolds number. The result of the left jet, which is similar to that of the right one, is presented. To eliminate the influence of the impingement wall, the values of

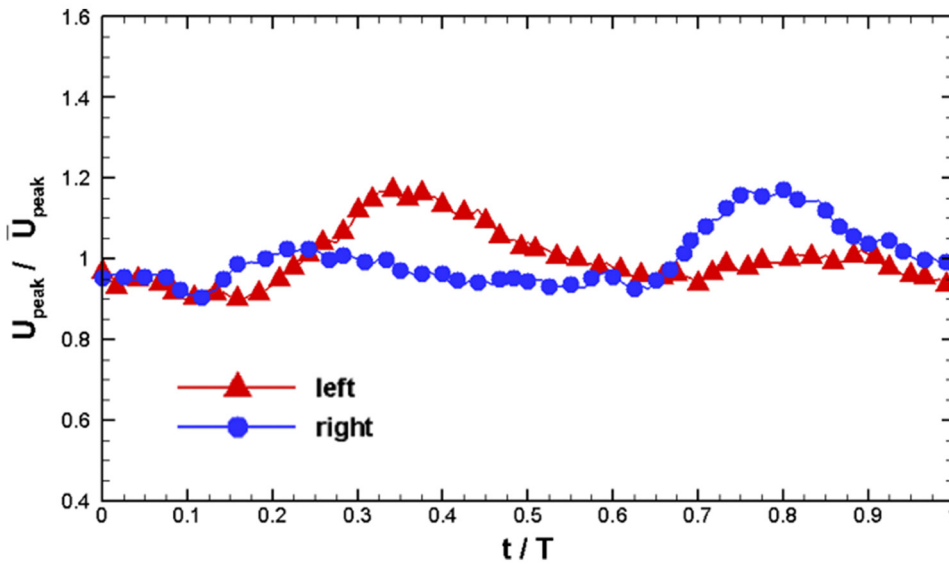
the two parameters are obtained in the near-exit region within  $x < 2D_h$ . As shown in Fig. 4(a), the maximum spreading angle  $\theta_{max}$  generally increases with the Reynolds number at first, until achieving a value of about  $\theta_{max} = 85^\circ$  at  $Re = 9.2 \times 10^3$ . The jet's spreading angle (up to  $85^\circ$ ) indicates that its sweeping motion is under considerable constraint of the exit geometry ( $100^\circ$ ). This result confirms that the current optimized design can effectively increase the jet maximum spreading angle with an approximately 100% increment compared to that obtained from the original design of Tomac and Gregory (2017). Figure 4(b) plots the Strouhal number  $St$  against the Reynolds number. The Strouhal number is defined as

$$St = \frac{fD_h}{U_{SJ}}, \quad (1)$$

where  $f$  is the jet oscillation frequency and  $U_{SJ}$  is the jet exit velocity. Opposite to the spreading angle,  $St$  decreases with the increase in the Reynolds number, until achieving convergence after approximately  $Re = 5.5 \times 10^3$ . The dependencies of the maximum spreading angle and the frequency against the



(a)



(b)

FIG. 6. Phase-resolved oscillation patterns of each jet: spreading angle (a) and peak velocity magnitude (b) in the near-exit region at  $Re = 1.8 \times 10^3$ . The differences between the jet angles are absolute values.

Reynolds number are similar to those found in single sweeping jets (Wen and Liu, 2018) that are rooted in flow interactions inside the oscillator.

The interactions between the dual sweeping jets are presented for three selected Reynolds numbers: the minimum  $Re = 1.8 \times 10^3$ , the intermediate  $Re = 5.5 \times 10^3$ , and the maximum  $Re = 9.2 \times 10^3$ . At the lowest Reynolds number, both jets have a smallest spreading angle and cannot impinge

directly on the centerline between the two jets. At the intermediate Reynolds number, the jets can just touch the centerline at a certain phase. At the highest Reynolds number, the jets can even pass the centerline. To better illustrate the unsteady flow fields, animations including line integral convolution (LIC) (Wen and Liu, 2018) streamlines and velocity magnitude at these three Reynolds numbers are available in videos 1–3 in the [supplementary material](#).

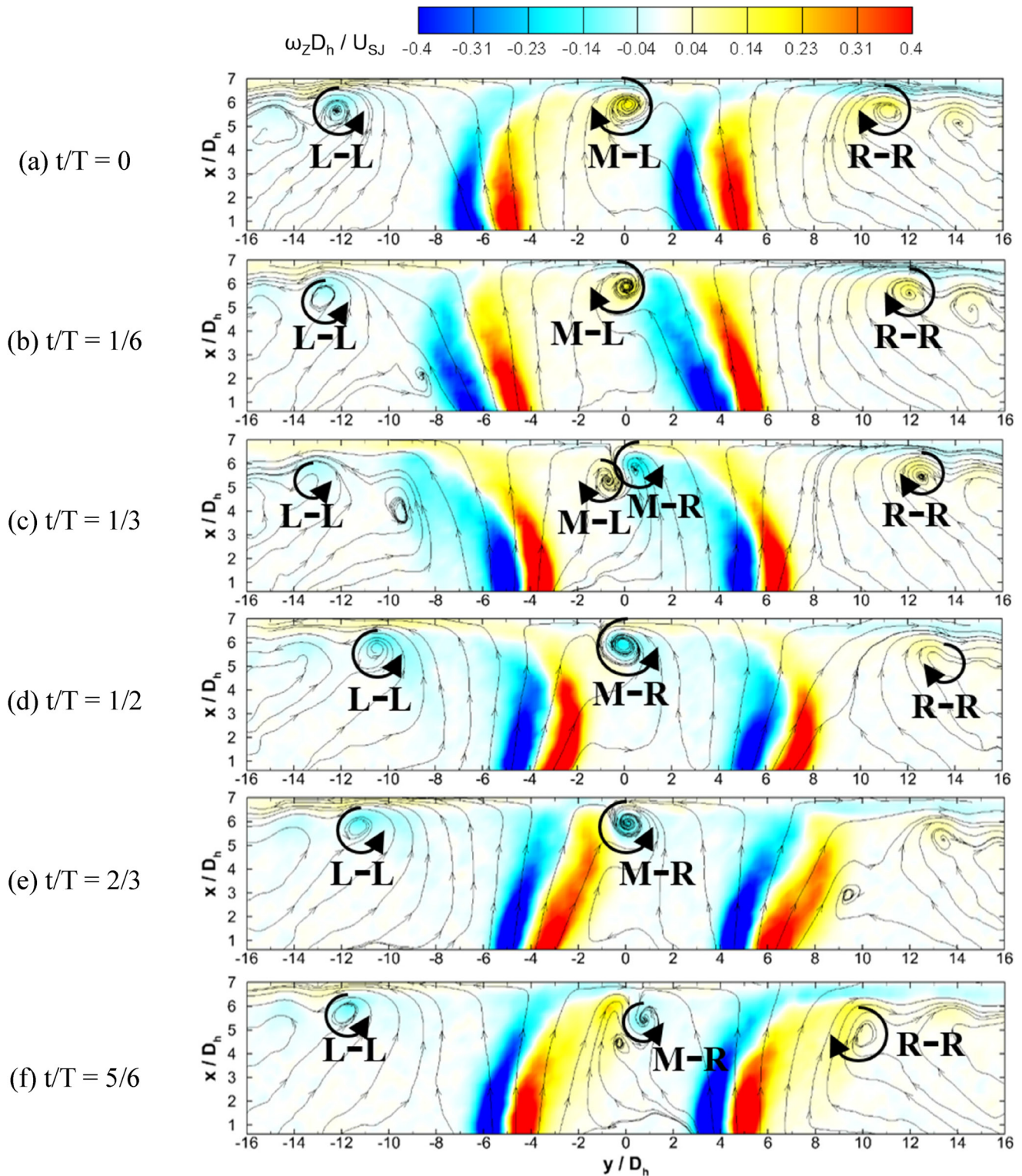


FIG. 7. Development and interactions of wall vortices shown by the contours of vorticity with streamlines at  $Re = 1.8 \times 10^3$ .

### B. $Re = 1.8 \times 10^3$

Figure 5 presents the contours of the phase-averaged velocity magnitude with streamlines during one cycle to show the flow dynamics of the dual sweeping impinging jets at the lowest Reynolds number. From the contours of the jet velocity magnitude, it can be seen that both jets have a small maximum spreading angle but smooth oscillation patterns, following a good in-phase oscillating motion. The velocity of each jet is also relatively stable with only mild variations from phase to phase. The topologies of the jet flows are similar to each other and can be generally treated as two isolated flows. However, interesting interactions between the jets are still indicated by streamlines in the near-wall region ( $x > 5D_h$ ). Wall vortices are induced by jet impingements both on the lateral outer sides of the whole flow field ( $|y| > 4.7D_h$ ) and in the middle region

around the centerline between the jets (around  $y = 0$ ). These vortices are examined in detail later.

To further quantitatively examine the oscillation patterns of each jet, Fig. 6 presents the phase-resolved jet spreading angle and the jet peak velocity extracted in the near-exit region during one cycle. As shown in Fig. 6(a), the sweeping motion of each jet generally follows sinusoidal and smooth patterns. However, small asymmetrical patterns can also be seen. Both jets have a larger spreading angle when these are deflected to the lateral outer sides than in the middle region. This causes small differences between the two jet motions. For example, at the beginning of the first half cycle, both jets are deflected to their most leftward positions. However, the left jet is on the left outer side of the whole flow field, whereas the right one is in the middle region. Therefore, the left jet has a larger angle than the right one does, leading to a motion difference close to 20% of

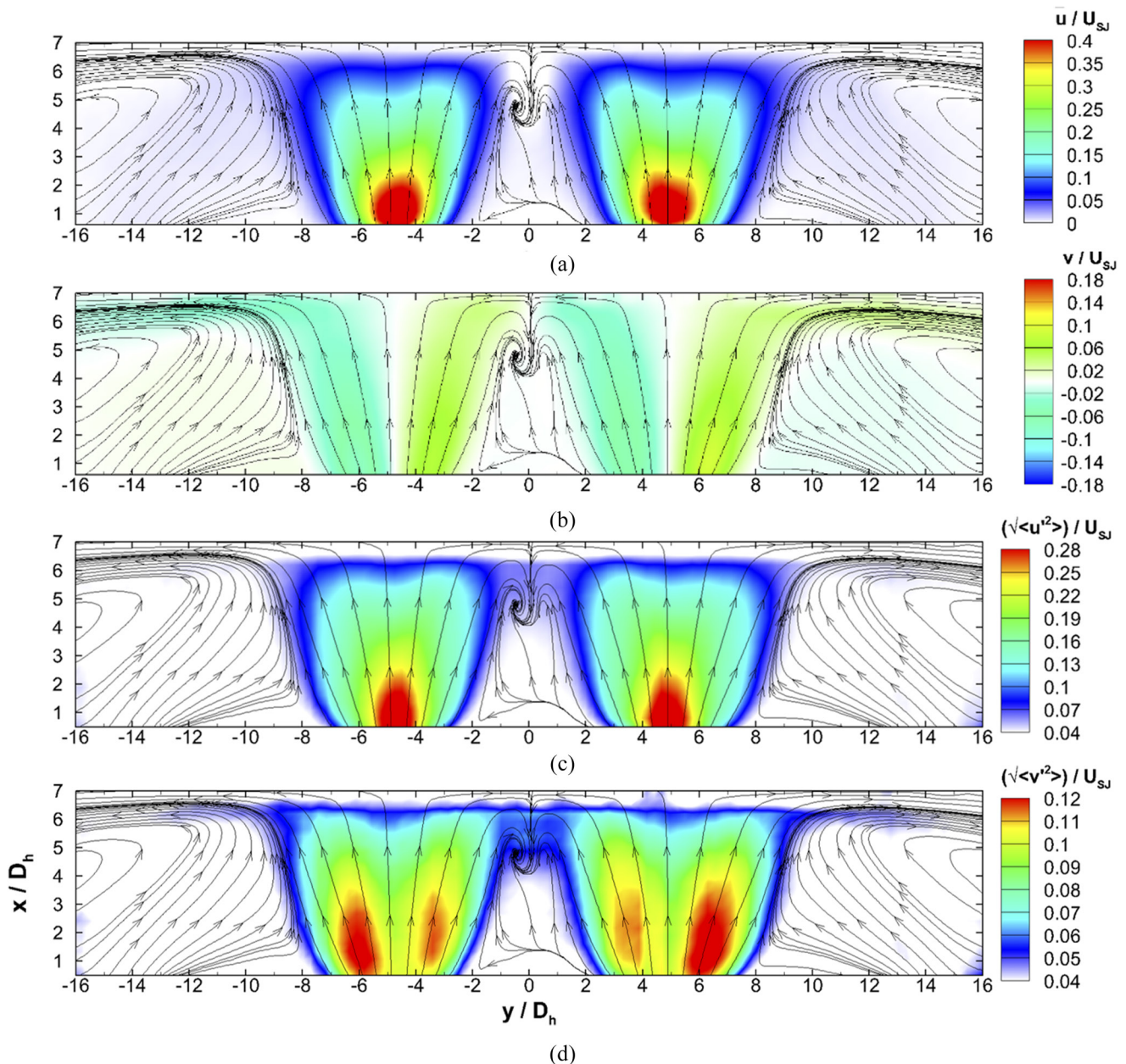


FIG. 8. Contours of time-averaged streamwise (a) and transverse velocity (b), and contours of correspondingly turbulent fluctuations [(c) and (d)] at  $Re = 1.8 \times 10^3$ .

the maximum jet spreading angle. At the beginning of the next half cycle, the situations are reversed but also lead to a maximum difference with a similar magnitude. Note that the motion difference is an absolute value in Fig. 6(a). Figure 6(b) presents the profiles of jet peak velocities. It shows that although the jet velocity magnitude is generally stable, it experiences

phase-to-phase variations during one actuation cycle with an amplitude of about 20% of the time-averaged mean value. Interestingly, the velocity changes of each jet are closely correlated. The velocity of the left jet has a peak value at about  $t/T = 0.35$ , whereas the right one has a peak value about one half cycle later at  $t/T = 0.8$ . Previous numerical results

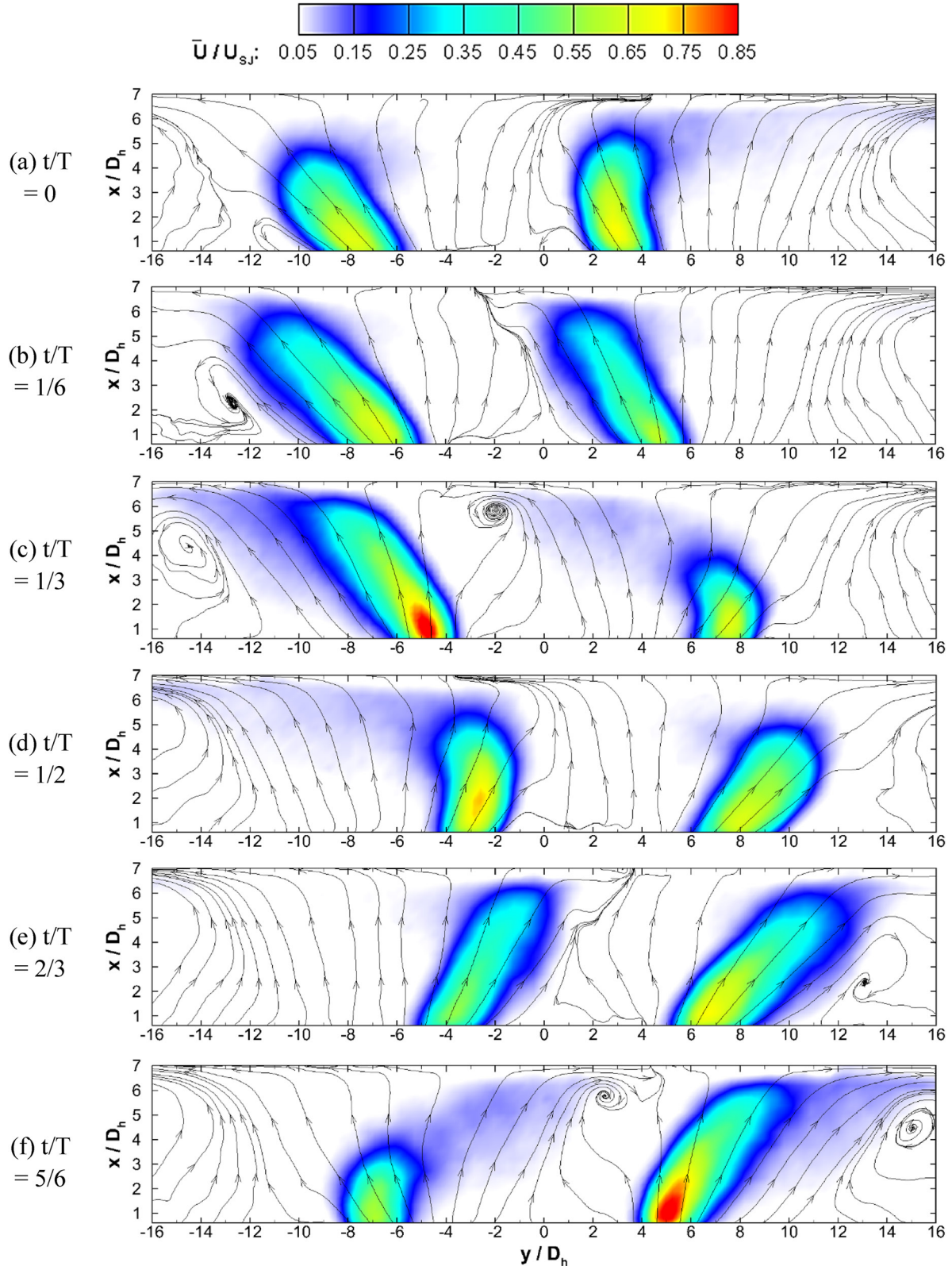


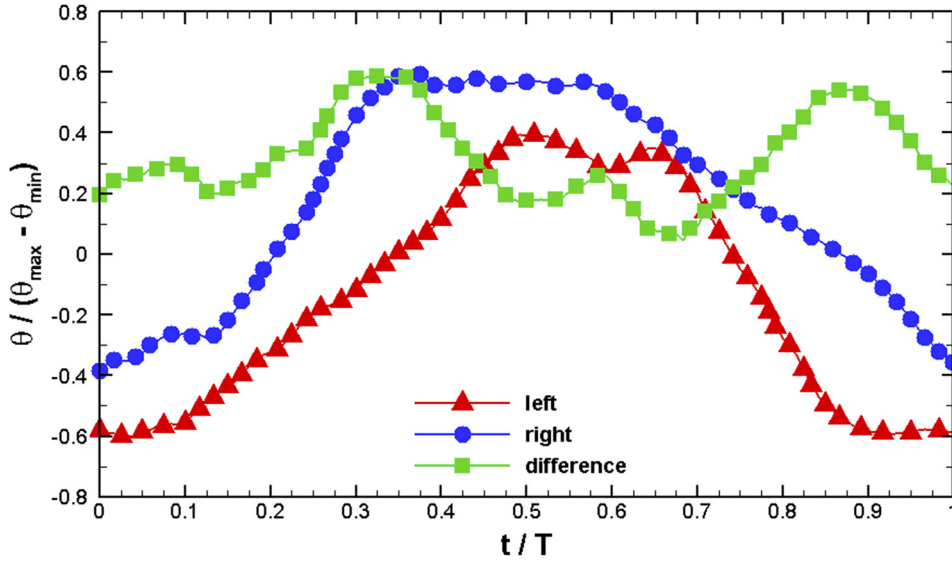
FIG. 9. Sweeping motions of the dual jets shown by the contours of the phase-averaged velocity magnitude with streamlines at  $Re = 5.5 \times 10^3$ .

(Tomas and Gregory, 2017) revealed flow exchanges inside the oscillator pair, which could be the reason for the correlated behavior. During the first half of the oscillation cycle, part of flow inside one actuator was observed to pass through the shared feedback channel and added into the jet flow issued from the other actuator. The internal flow direction was reversed in the other half cycle. This periodic internal flow exchange could lead to the close correlated peak velocities of the dual sweeping jets.

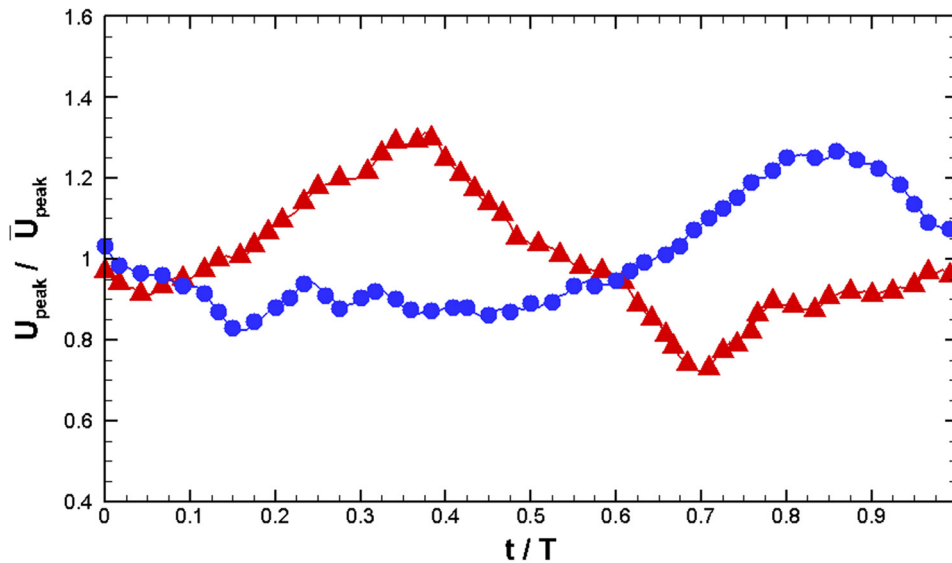
As mentioned above, to reveal detailed interactions between the wall vortices, contours of vorticity with streamlines are plotted. The results are presented in Fig. 7, in which the highlighted regions with wall vortex cores identified by the streamlines reveal formations of wall vortices on the lateral outer sides and trade-off interactions between them in the middle region. The value of vorticity indicates the rotation direction of the wall vortices. For concise notation, the wall vortex induced by the left jet on the left outer side is termed “L-L,” and “M-L” indicates the vortex induced in

the middle region. Similarly, the outer and middle vortices induced by the right jet are indicated by “R-R” and “M-R,” respectively.

As shown in Fig. 7(a), the jet column is captured by the pair of high vorticity strips. Three coherent wall vortices are identified at the beginning of the cycle, i.e.,  $t/T = 0$ . At this point, both jets are sweeping from the right side to the left side in the near-wall region. Therefore, the left jet produces a pair of counter-rotating wall vortices, “L-L” and “M-L.” The “M-L” vortex is newly generated, while the “L-L” vortex is generated in the preceding cycle. In contrast, the right jet only produces one “R-R” vortex on the right outer side. The “M-R” vortex generated in the preceding cycle is destroyed by the left jet. As time increases to  $t/T = 1/6$ , as shown in Fig. 7(b), both of the lateral vortices, “L-L” and “R-R,” are traveling further outside and losing strength due to dissipation and possible stretching in the out-of-plane direction. The “M-L” vortex in the middle region is also interrupted by the right jet, which is approaching its leftmost position and has opposite vorticity values.



(a)



(b)

FIG. 10. Phase-resolved oscillation patterns of each jet: spreading angle (a), and peak velocity magnitude (b) in the near-exit region at  $Re = 5.5 \times 10^3$ . The differences between the jet angles are absolute values.

At  $t/T = 1/3$ , as shown in Fig. 7(c), the lateral vortices further reduce in strength and are almost unidentifiable. In the middle region, the “M-L” vortex is further weakened. On the other hand, a new vortex, “M-R,” begins to form by the right jet, which is located close to the “M-L” vortex but with an opposite sense of rotation. At half cycle  $t/T = 1/2$ , as shown in Fig. 7(d), the “M-L” vortex disappears due to the strong

interruption of the right sweeping jet, leaving only the “M-R” vortex in the middle region. At the same time, as the left jet is deflected to its leftmost position in the near-wall region, a new “L-L” vortex is formed. In the following half cycle, the vortex interactions are very similar to those in the first half but are flipped according to the middle centerline of the whole flow field, as shown in Figs. 7(e) and 7(f).

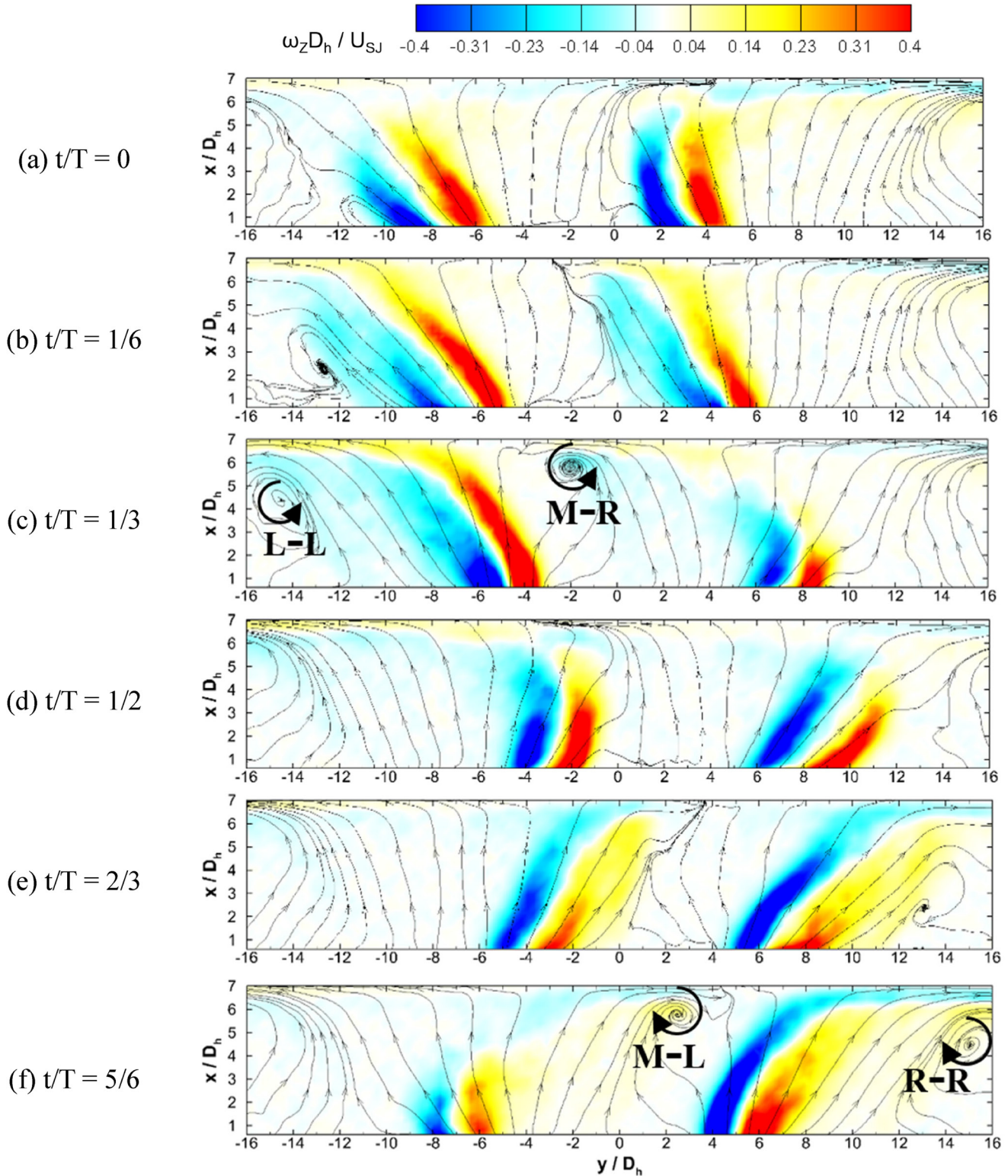


FIG. 11. Development and interactions of wall vortices shown by contours of vorticity with streamlines at  $Re = 5.5 \times 10^3$ .

The time-averaged impingement effect is also affected by the oscillation patterns and wall vortices. As shown by the contour of streamwise velocity in Fig. 8(a), both jets produce an enlarged area of impingement due to their sweeping motions along the wall. However, as a result of the small jet maximum spreading angle, the two jets are clearly separated by a large gap of up to  $2D_h$  between them. From the streamlines, it can be seen that the gap is filled by an upwash flow, which is induced by the wall vortices. As dual jets can generally be treated as two isolated jets, each generates one major region of high streamwise velocity close to the wall. Within each region, there are two local peaks with a low-velocity region in between, due to the deflected jet column of single sweeping jets (Wen *et al.*, 2018). As shown in Fig. 8(b), the magnitude of transverse velocity is only about half that of the streamwise velocity in the near-exit region. This is

because the jet momentum is more streamwise due to the small maximum spreading angle. However, in the near wall region, both velocity components have similar magnitudes. For the transverse velocity, each jet has one pair of positive and negative peak values accordingly. In the middle region between the two jets around the centerline, both velocity components have a lower value because the jets cannot directly impinge on the centerline (Wen *et al.*, 2017). However, the contours of turbulent fluctuations show some differences, especially in the transverse direction in the middle region of the two jets. The turbulence fluctuations are obtained through the application of the triple decomposition, which is commonly used in the studies of jet impingement (Greco *et al.*, 2016 and Wen *et al.*, 2018). Using this method, instantaneous velocity is decomposed into a time-averaged velocity component, phase-correlated velocity, and turbulent fluctuation.

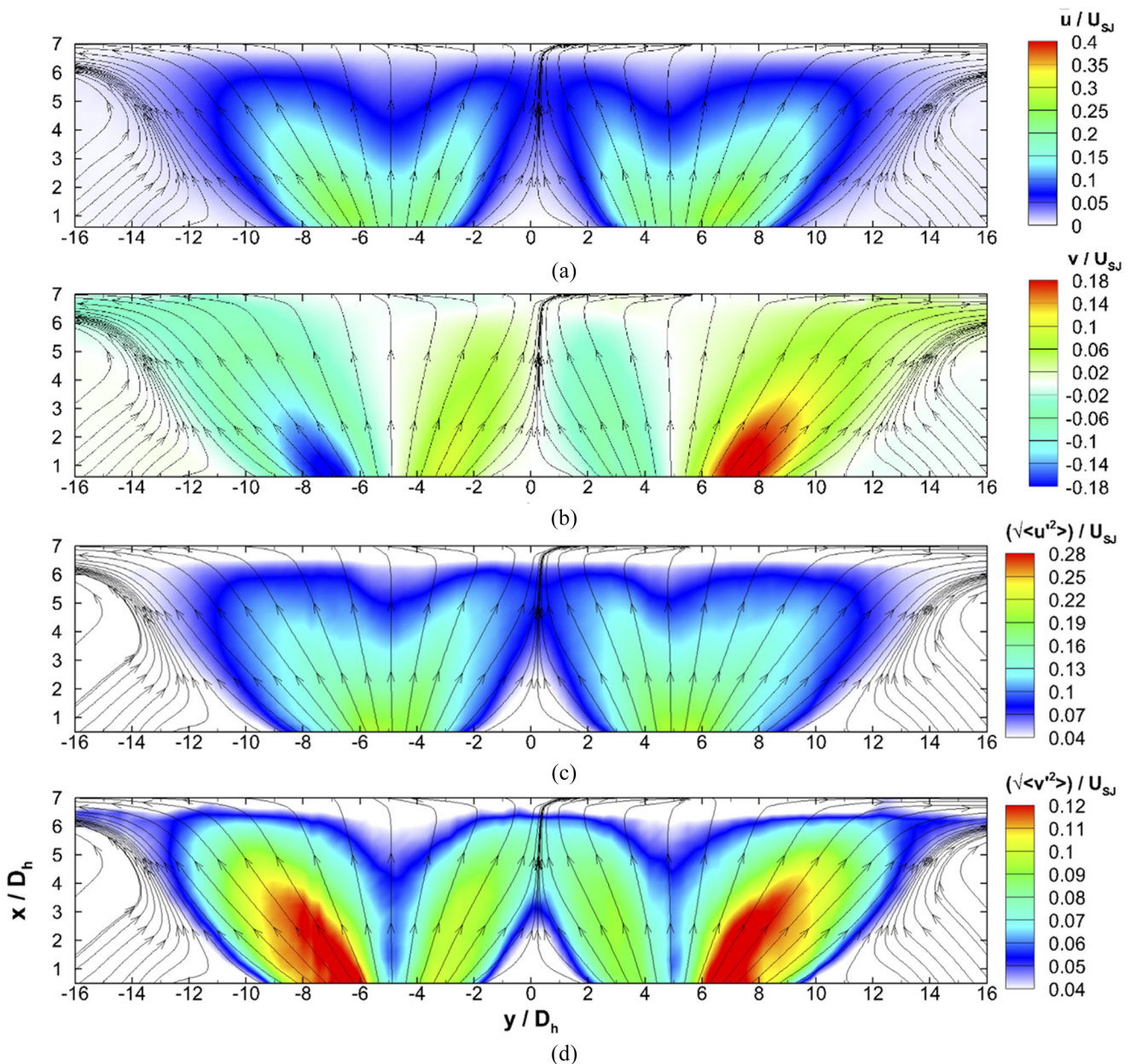


FIG. 12. Contours of time-averaged streamwise (a) and transverse velocity (b), and contours of correspondingly turbulent fluctuations [(c) and (d)] at  $Re = 5.5 \times 10^3$ .

To characterize the turbulence intensity, the root-mean-squared value is computed from the velocity fluctuations. As shown in Figs. 8(c) and 8(d), remarkably high turbulence fluctuations are observed in the middle region around the centerline, especially in the transverse direction, as a result of the wall vortex interactions. Therefore, the transverse velocity has

a more uniform distribution along the wall than its counterpart in the streamwise direction.

### C. $Re = 5.5 \times 10^3$

Figure 9 presents the phase-averaged velocity magnitude with streamlines at  $Re = 5.5 \times 10^3$ . Compared to those at

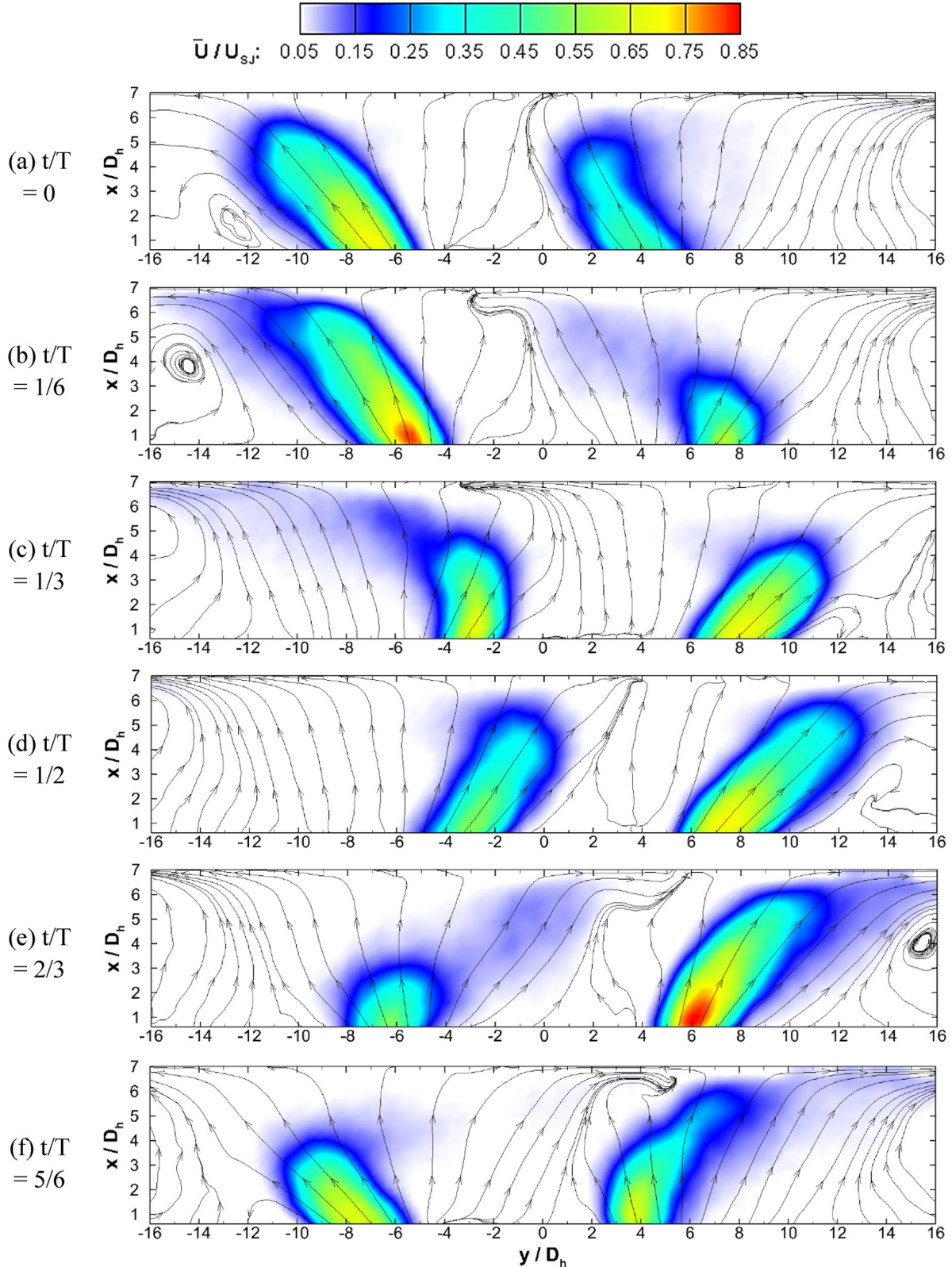


FIG. 13. Sweeping motions of the dual jets shown by contours of phase-averaged velocity magnitude with streamlines at  $Re = 9.2 \times 10^3$ .

the lowest Reynolds number, both jets have a larger maximum spreading angle and can therefore directly impinge on the middle region around the centerline at certain phases, i.e.,  $t/T = 1/6$  and  $2/3$ . However, the oscillation patterns are distorted to some extent. First, the two jets are unable to maintain good in-phase motions. For example, at  $t/T = 1/3$ , the left jet is mostly at its leftmost position, whereas the right jet is approaching its rightmost position in the near-exit region. Second, the phase-resolved jet velocity experiences strong variations during one cycle. In general, the jet velocity is higher when it is deflected to the lateral outer sides than in the middle region.

These changes are shown more clearly in the plot of phase-resolved sweeping motions and jet velocity magnitude of the dual jets in Fig. 10. As shown in Fig. 10(a), the in-phase sweeping motion between the two jets is significantly interrupted and experiences a large difference of up to 60% of the jet maximum spreading angle. This large motion difference has two major causes. First, similar to the results observed at the lowest Reynolds number, the jet has a larger spreading angle on the outer side than in the middle region. However, as shown by the phase-resolved spreading angles of each jet, this only contributes about 30% of the total motion difference. The other reason is that both jets sweep faster from the middle region to the lateral outer sides than these sweep back in the reverse route. For example, in the first half cycle, the right jet sweeps

from the middle region at  $t/T = 0$  and reaches its rightmost position on the right outer side of the whole flow field at about  $t/T = 0.3$ . The left jet sweeps from the left outer side and reaches its rightmost position in the middle region much later at about  $t/T = 0.5$ . Therefore, the distorted jet sweeping motion eventually contributes about 70% of the total motion difference. It is also interesting to note that the motion difference has two peak values at about  $t/T = 0.35$  and  $0.85$ , closely correlated with a phase difference of about half a cycle.

The velocity magnitude of both jets also experiences high and closely correlated phase-to-phase variations. As shown in Fig. 10(b), the peak velocity profile of each jet has one pair of positive and negative peak values with a variation amplitude of about 30% of the mean velocity. By correlation with the jet sweeping motion, it is found that each jet has a maximum velocity when the majority of the jet is deflected to the lateral outer side, and a minimum velocity when the jet is in the middle region. Therefore, the phase-to-phase variations of the jet velocity are also closely correlated between the dual jets with a phase difference of about  $0.5 T$ . The strong and closely correlated changes in the jet oscillation patterns indicate that the dual sweeping jets would be better treated as a whole system rather than as two isolated ones.

Wall vortices captured by the streamlines and vorticity contours also change according to phase-resolved jet sweeping

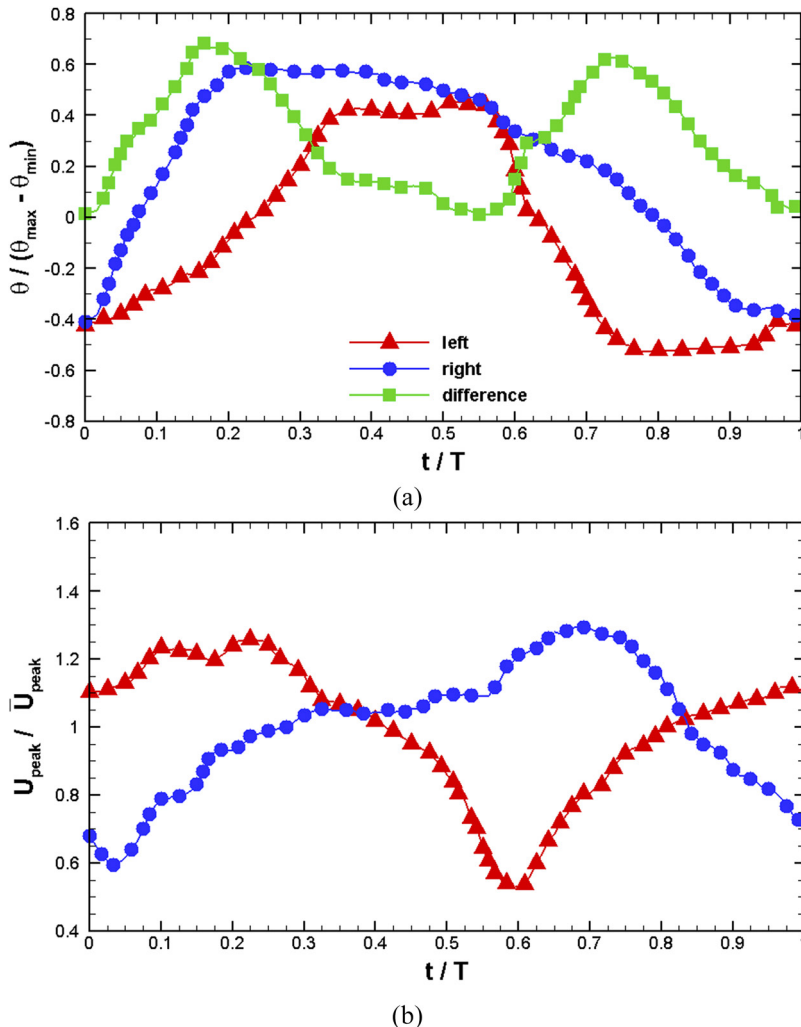


FIG. 14. Phase-resolved oscillation patterns of each jet: spreading angle (a), and peak velocity magnitude (b) in the near-exit region at  $Re = 9.2 \times 10^3$ . The differences between the jet angles are absolute values.

motion and jet velocity variations, especially in the middle region. As shown in Fig. 11, the lateral wall vortices are still induced on the outer sides as indicated by “L-L” and “R-R.” However, the wall vortices in the middle region are much weaker. During the whole cycle, an “M-R” vortex and an “M-L” vortex are only identified at  $t/T = 1/3$  and  $5/6$ , respectively. There are two probable reasons for this observation.

First, due to the enlarged jet sweeping motion, there is less space and time for the development of wall vortices. The wall vortex induced by one jet is more likely to be destroyed by the other jet because the sweeping jets can directly impinge on the middle region. Second, the strength of wall vortices reduces because the jets become weaker when these are deflected into the middle region.

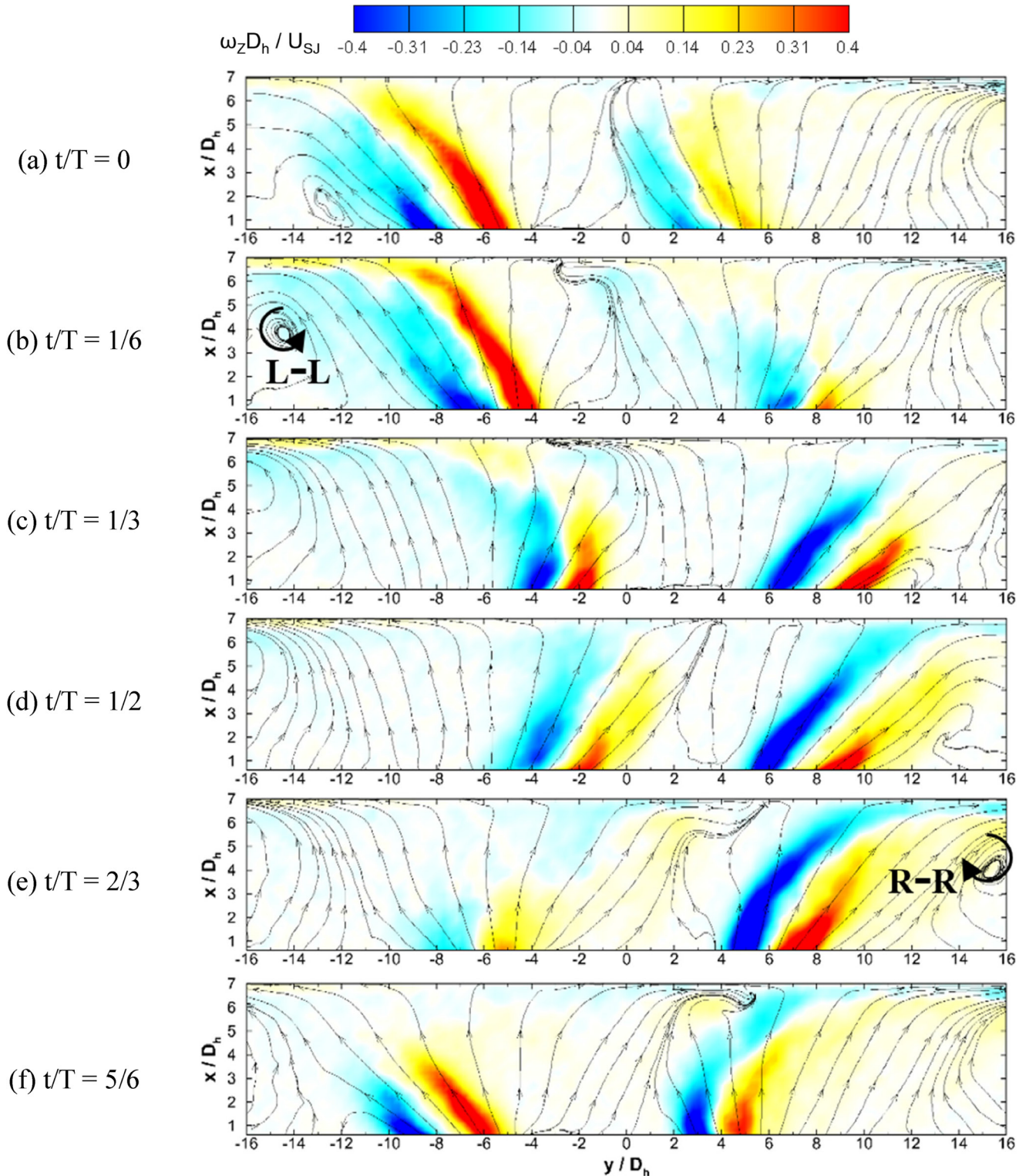


FIG. 15. Development and interactions of wall vortices shown by contours of vorticity with streamlines at  $Re = 9.2 \times 10^3$ .

The time-averaged impingement effect changes accordingly. As shown in Figs. 12(a) and 12(b), the branch of each jet in the middle region is clearly weaker than its counterpart on the lateral outer side. In addition, due to the enlarged jet maximum spreading angle, a large low-velocity region is generated between the two branches of each jet, as shown in Fig. 12(a). In the middle region between the two jets, the upwash flow observed at the lowest Reynolds number disappears due to the weak wall vortices. Therefore, in the region close to the wall, the streamwise velocity has three major high-value regions. Two regions are at the lateral outer sides, while one is in the middle region around the centerline of the two jets. Between the three high-value regions, two regions with low velocity are formed. As shown in Fig. 12(b), the transverse velocity, in contrast, only has one pair of positive and negative peak values

laterally because the inner branches of the two jets collide and cancel out the transverse velocity in the middle region around the centerline. Despite the low values for time-averaged velocity, periodic jet impingement can still lead to strong turbulence fluctuations in the middle region, as shown in Figs. 12(c) and 12(d). Therefore, both the streamwise and transverse turbulent fluctuations have three major high-value regions close to the wall. Similar to the streamwise velocity results, two peaks can be seen at the lateral outer sides, while one is in the middle region.

#### D. $Re = 9.2 \times 10^3$

Both jets have the largest maximum spreading angles at the maximum Reynolds number. As shown by the

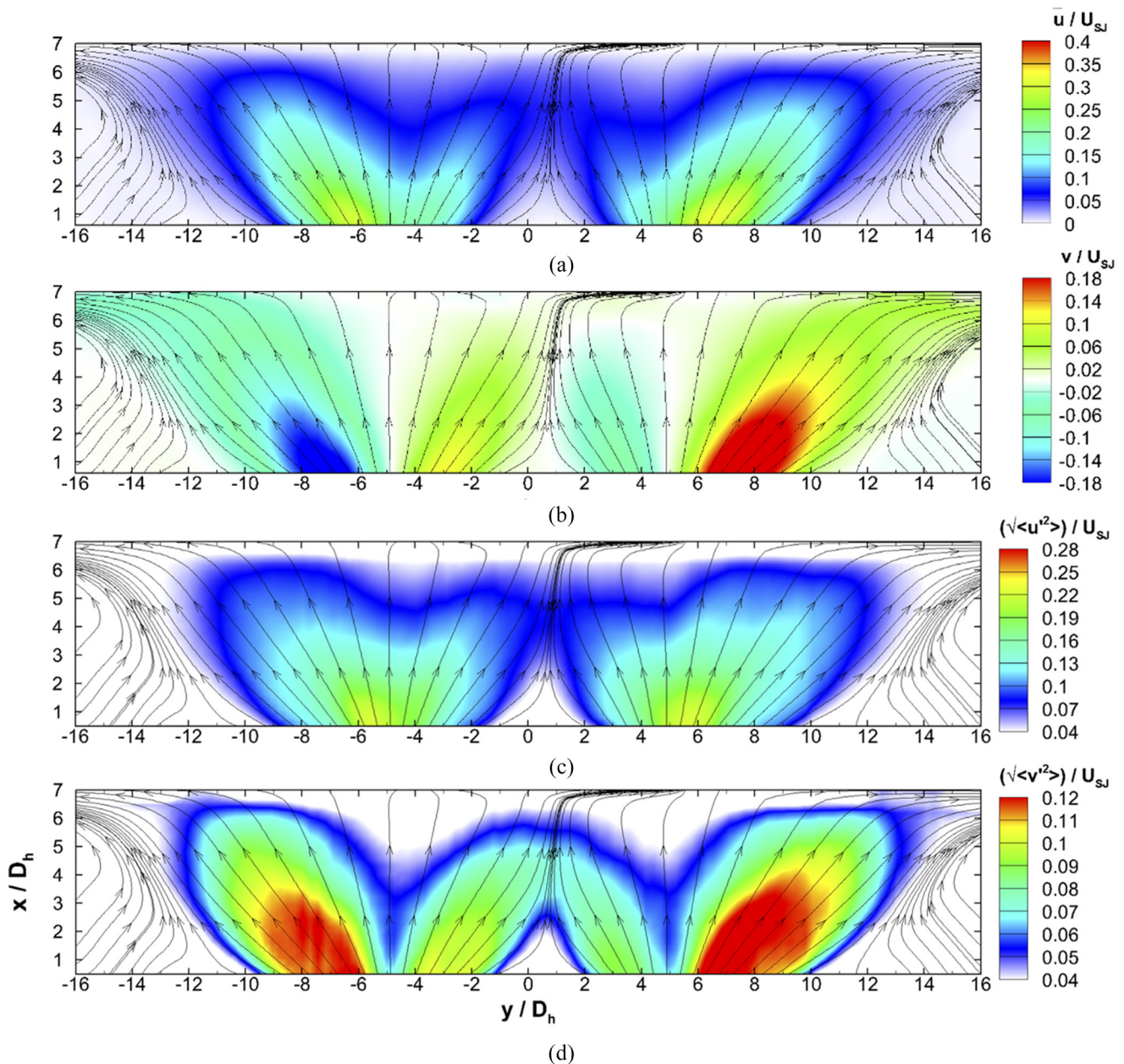


FIG. 16. Contours of time-averaged streamwise (a) and transverse velocity (b), and contours of correspondingly turbulent fluctuations [(c) and (d)] at  $Re = 9.2 \times 10^3$ .

phase-averaged flow fields in Fig. 13, each jet can even pass the middle region to impinge on the other side at certain phases, i.e.,  $t/T = 1/6$  and  $2/3$ . However, the oscillation patterns of the dual jets are mostly distorted. The dual jets have a large difference between their sweeping motions and experience high variations in their phase-resolved jet velocity. As shown more clearly in Fig. 14(a), the difference between their sweeping motions can be up to 70% of the jet maximum spreading angle because the sweeping speed of each jet changes more significantly within one cycle. For example, it only takes the right jet from  $t = 0$  to  $0.2 T$  to sweep from the middle region to the right outer side. It then stays on the outer side for a long time, until about  $t/T = 0.5$ , when it begins to sweep back. The speed then becomes much lower, and the jet takes about half a cycle to sweep back. The left jet is just the opposite. This eventually leads to a large difference between the two jet sweeping motions. It is notable that even though the in-phase motion is significantly interrupted, there is no direct collision between the dual jets. Figure 14(b) shows that jet velocity magnitude also has strong variations from phase to phase with an amplitude of up to 50% of the mean value. Similar to the observations at the intermediate Reynolds number but to a greater extent, each jet has a higher velocity on the outer side than in the middle region. As such, the dual-jet system behaves similar to the sweeping jet that would be produced from a single, but larger, actuator. In the near-wall region, due to the large jet maximum spreading angle and weak jet in the middle region, wall vortices are hardly identifiable throughout the whole cycle. As shown in Fig. 15, the wall vortices are only captured alternately on both outer sides, just like those produced by a single, but larger, sweeping jet. The time-averaged flow fields and turbulent fluctuations change accordingly. As shown in Fig. 16, both the streamwise and transverse velocity components are more directed toward the lateral outer sides than into the middle region. Therefore, all velocity components and turbulent fluctuations have peak values laterally along the wall and have a large proportion of low values in the middle region around the centerline of the two jets.

#### IV. CONCLUSIONS

This paper documents detailed flow dynamics associated with dual sweeping jets impinging upon a flat wall for Reynolds numbers ranging from  $1.8 \times 10^3$  to  $9.2 \times 10^3$ . The exit-to-wall distance is fixed at  $7D_h$ . The TR-PIV results are assessed to provide a detailed examination of the oscillation patterns of the dual jets and interactions of induced wall vortices at three selected Reynolds numbers. In addition, overall impingement effects are examined by time-averaged flow fields and turbulence fluctuations. In general, three distinct behaviors of the dual jets are observed.

At the lowest Reynolds number  $Re = 1.8 \times 10^3$ , both jets follow a similar sinusoidal motion with good in-phase sweeping. The jet velocity magnitude is also stable with only mild variations from phase to phase during one actuation cycle. At the smallest jet spreading angle, both jets cannot directly impinge on the middle region around the centerline of the two jets. However, one pair of counter-rotating wall vortices is

induced alternatively in the middle region. The time-averaged wall vortices also produce an upwash flow. Separated by the upwash flow, each jet produces a region of high-value time-averaged streamwise velocity and its turbulence fluctuations laterally along the wall. The transverse velocity has one pair of positive and negative peak values laterally along the wall. Interestingly, the transverse turbulence fluctuation has high values in the middle region, which is caused by interactions between the wall vortices. In general, the dual sweeping impinging jets can be treated as two isolated jets with wall vortex interactions between them.

At the highest Reynolds number  $Re = 9.2 \times 10^3$ , the sweeping motion of each jet is significantly distorted. The jet sweeps much faster when it moves from the middle region to the lateral outer sides of the whole flow field than when it sweeps back. This leads to a significant interruption of the in-phase motion. Jet velocity magnitude also experiences strong variation from phase to phase. Both jets have much higher velocity when these are on the outer sides than in the middle region. Wall vortices are hardly identifiable in the middle region. Accordingly, all of the time-averaged velocity components and turbulence fluctuations close to the wall have peak values only laterally along the wall on the outer sides and have much lower values in the middle region. Therefore, the dual jets are, in essence, very similar to the sweeping jet that would be produced from a single, but bigger, oscillator.

At the intermediate Reynolds number  $Re = 5.5 \times 10^3$ , the oscillation patterns and performance of wall vortices are at a transition stage. Time-averaged profiles of velocity components and turbulence fluctuations generally have three peak values along the wall. Two peaks are on the lateral outer sides and one is in the middle region. One exception is the transverse velocity, which only has peak values laterally along the wall because the transverse velocity is canceled out in the middle region.

The current investigation shows that dual sweeping jets can provide a more uniform impingement at lower Reynolds numbers than at the highest Reynolds number. Besides the Reynolds number, it is also interesting to investigate the effect of the exit-to-wall distance, although this was fixed in the current study. By moving the wall closer to the exits, dual sweeping jets are expected to have less coverage along the wall. The interactions observed at the intermediate Reynolds number may occur at an even lower Reynolds number with a shorter exit-to-wall distance.

#### SUPPLEMENTARY MATERIAL

See [supplementary material](#) for a better illustration of the unsteady flow fields: animations including line integral convolution (LIC) (Wen and Liu, 2018) streamlines and velocity magnitude (see videos 1–3) at the three Reynolds numbers  $Re = 1.8 \times 10^3$ ,  $5.5 \times 10^3$ , and  $9.2 \times 10^3$ , respectively.

#### ACKNOWLEDGMENTS

The authors gratefully acknowledge financial support for this study from the National Natural Science Foundation of China (Grant Nos. 11702172 and 11725209).

- Agricola, L., Hossain, M. A., Prenter, R., Lundgreen, R., Ameri, A., Gregory, J., and Bons, J. P., "Impinging sweeping jet heat transfer," *AIAA Paper* 2017-4974, 2017.
- Bobusch, B. C., Wozidlo, R., Bergada, J. M., Nayeri, C. N. N., and Paschereit, C. O., "Experimental study of the internal flow structures inside a fluidic oscillator," *Exp. Fluids* **54**(6), 1559 (2013).
- Camci, C. and Herr, F., "Forced convection heat transfer enhancement using a self-oscillating impinging planar jet," *J. Heat Transfer* **124**(4), 770–782 (2002).
- Can, M., "Experimental optimization of air jets impinging on a continuously moving flat plate," *Heat Mass Transfer* **39**, 509–517 (2003).
- Chander, S. and Ray, A., "Heat transfer characteristics of three interacting methane/air flame jets impinging on a flat surface," *Int. J. Heat Mass Transfer* **50**, 640–653 (2007).
- Chatterjee, A. and Fabris, D., "Planar non-Newtonian confined laminar impinging jets: Hysteresis, linear stability, and periodic flow," *Phys. Fluids* **29**, 103103 (2017).
- Fairweather, M. and Hargrave, G., "Experimental investigation of an axisymmetric, impinging turbulent jet. I: Velocity field," *Exp. Fluids* **33**(3), 464–471 (2002).
- Farahani, S. D., Bijarchi, M. A., Kowsary, F., and Ashjaee, M., "Optimization arrangement of two pulsating impingement slot jets for achieving heat transfer coefficient uniformity," *J. Heat Transfer* **138**(10), 102001 (2016).
- Feng, L. H. and Wang, J. J., "The virtual aeroshaping enhancement by synthetic jets with variable suction and blowing cycles," *Phys. Fluids* **26**(1), 014105 (2014).
- Feng, L. H., Wang, J. J., and Pan, C., "Proper orthogonal decomposition analysis of vortex dynamics of a circular cylinder under synthetic jet control," *Phys. Fluids* **23**(1), 014106 (2011).
- Geers, L. F. G., Tummers, M. J., and Hanjalić, K., "Particle imaging velocimetry-based identification of coherent structures in normally impinging multiple jets," *Phys. Fluids* **17**(5), 055105 (2005).
- Greco, C. S., Castrillo, G., Crispo, C. M., Astarita, T., and Cardone, G., "Investigation of impinging single and twin circular synthetic jets flow field," *Exp. Therm. Fluid Sci.* **74**, 354–367 (2016).
- Guo, T., Rau, M. J., Vlachos, P. P., and Garimella, S. V., "Axisymmetric wall jet development in confined jet impingement," *Phys. Fluids* **29**, 025102 (2017).
- Hadžiabdić, M. and Hanjalić, K., "Vortical structures and heat transfer in a round impinging jet," *J. Fluid Mech.* **596**, 221–260 (2008).
- Hewakandamby, B. N., "A numerical study of heat transfer performance of oscillatory impinging jets," *Int. J. Heat Mass Transfer* **52**, 396–406 (2009).
- Hubble, D., Vlachos, P. P., and Diller, T. E., "The role of large-scale vortical structures in transient convective heat transfer augmentation," *J. Fluid Mech.* **718**, 89–115 (2013).
- Koklu, M., "Effect of a Coanda extension on the performance of a sweeping-jet actuator," *AIAA J.* **54**(3), 1131–1134 (2016).
- Lundgreen, R. K., Hossain, A. F., Prenter, R., Bons, J. P., Gregory, J. W., and Ameri, A., "Impingement heat transfer characteristics of a sweeping jet," *AIAA Paper* 2017-1535, 2017.
- New, T. H. and Long, J., "Dynamics of laminar circular jet impingement upon convex cylinders," *Phys. Fluids* **27**, 024109 (2015).
- Ostermann, F., Wozidlo, R., Gaertlein, S., Nayeri, C. N., and Paschereit, C. O., "Phase-averaging methods for the natural flow field of a fluidic oscillator," *AIAA J.* **53**(8), 2359–2368 (2015).
- Park, T., Kara, K., and Kim, D., "Flow structure and heat transfer of a sweeping jet impinging on a flat wall," *Int. J. Heat Mass Transfer* **124**, 920–928 (2018).
- Raffel, M., Willert, C. E., and Kompenhans, J., *Particle Image Velocimetry: A Practical Guide* (Springer, Berlin, 2013).
- Terzis, A., "On the correspondence between flow structures and convective heat transfer augmentation for multiple jet impingement," *Exp. Fluids* **57**(9), 146 (2016).
- Tesař, V., "Enhancing impinging jet heat or mass transfer by fluidically generated flow pulsation," *Chem. Eng. Res. Des.* **87**(2), 181–192 (2009).
- Tesař, V., "Impinging jets," in *Vortex Rings and Jets: Recent Developments in Near-field Dynamics*, edited by New, D. T. H. and Yu, S. C. M. (Springer Singapore, Singapore, 2015).
- Tomac, M. N. and Gregory, J. W., "Phase-synchronized fluidic oscillator pair," *AIAA Paper* 2017-3314, 2017.
- Wen, X. and Liu, Y., "Lagrangian analysis of sweeping jets measured by time-resolved particle image velocimetry," *Exp. Therm. Fluid Sci.* **97**, 192–204 (2018).
- Wen, Z. X., He, Y. L., and Ma, Z., "Effects of nozzle arrangement on uniformity of multiple impinging jets heat transfer in a fast cooling simulation device," *Comput. Fluids* **164**, 83–93 (2017).
- Wen, X., Liu, Y., and Tang, H., "Unsteady behavior of a sweeping impinging jet: Time-resolved particle image velocimetry measurements," *Exp. Therm. Fluid Sci.* **96**, 111–127 (2018).
- Wen, X., Tang, H., and Duan, F., "Vortex dynamics of in-line twin synthetic jets in a laminar boundary layer," *Phys. Fluids* **27**(8), 083601 (2015).
- Wozidlo, R., Ostermann, F., Nayeri, C. N., and Paschereit, C. O., "The time-resolved natural flow field of a fluidic oscillator," *Exp. Fluids* **56**(6), 125 (2015).
- Vejrazka, J., Tihon, J., Marty, P., and Sobolik, V., "Effect of an external excitation on the flow structure in a circular impinging jet," *Phys. Fluids* **17**(10), 105102 (2005).
- Xu, Y., Feng, L. H., and Wang, J. J., "Experimental investigation of a synthetic jet impinging on a fixed wall," *Exp. Fluids* **54**(5), 1512 (2013).
- Xu, Y., He, G. S., Kulkarni, V., and Wang, J. J., "Experimental investigation of influence of Reynolds number on synthetic jet vortex rings impinging onto a solid wall," *Exp. Fluids* **58**, 6 (2017).
- Yadav, H. and Agrawal, A., "Effect of vortical structures on velocity and turbulent fields in the near region of an impinging turbulent jet," *Phys. Fluids* **30**, 035107 (2018).
- Yasuhiko, S., Shigeru, N., Taketoshi, O., and Koji, O., "A highly accurate iterative PIV technique using a gradient method," *Meas. Sci. Technol.* **11**(12), 1666 (2000).